# Solid-fluid interaction in porous materials with internal erosion

Wei Chen<sup>1</sup> · Yang Zhao<sup>2</sup> · Ronaldo I. Borja<sup>1,\*</sup>

- 1. Department of Civil and Environmental Engineering, Stanford University, Stanford, CA 94305, USA. \*E-mail: borja@stanford.edu
- 2. State Key Laboratory of Hydroscience and Engineering, Department of Hydraulic Engineering, Tsinghua University, Beijing 100084, China.

**Summary.** Various applications in science and engineering involve porous materials where the fluid erodes the solid either chemically or mechanically and transports the finer particles through the larger pore spaces of the residual solid. In soil mechanics, the process is called suffusion. In rocks, erosion is mainly due to chemical dissolution. Irrespective of the manner in which the solid erodes, the much finer particles mix with the pure fluid to form a thick fluid whose mass density is greater than that of the pure fluid but less than that of the intact solid. As the solid loses mass, its porosity increases and its mechanical properties degrade, thus impacting the deformation and fluid flow responses of the system. This paper formulates the complex kinematics and conservation equations governing the solid-fluid interaction with internal erosion. We use the classic  $\boldsymbol{u}/p$  formulation in which  $\boldsymbol{u}$  is the displacement of the residual solid and p is the pressure in the thick fluid. We focus on the case of chemical erosion in rocks where the eroded particles are so small that the interface between them and the pure fluid may be neglected. We then present numerical examples demonstrating the flow and deformation processes in porous materials subjected to internal erosion.

**Keywords.** Chemical dissolution, internal erosion, poroelasticity, suffusion.

## 1 Introduction

Internal erosion in geologic materials due to the interaction of pore fluid and solid grains is a commonly observed phenomenon in many natural processes and engineering applications [21, 22, 29, 43, 59]. Internal erosion in geologic materials can be categorized into two common types: suffusion, which is a type of erosion dominated by physical processes [26, 64], and solid dissolution, which is a process dominated by chemical reaction [42, 50, 52, 58]. Suffusion generally takes place in granular materials such as sands, where high-speed pore fluid flow carries finer particles away through the porous skeleton formed by coarser particles [46]. Solid dissolution refers to the phenomenon where reactive pore fluid dissolves soluble constituents in geologic materials through

chemical reaction. Internal erosion in geologic materials can have both positive and negative impacts on engineering practices. Richards and Reddy [56] investigated the causes of dam failures on a kilometer scale and concluded that for approximately half of cases, failure was associated with soil erosion. For carbon geological sequestration [35, 44, 54], solid dissolution in the shale caprock is a key factor that may impair the long-term integrity of the reservoir seal. Properly-leveraged internal erosion in geologic materials can also be beneficial for engineering applications. For instance, in shale gas exploitation, acids are usually pumped into the reservoir to weaken the rocks and improve the efficiency of hydraulic fracturing [24, 49, 65, 78].

The work introduced in this paper focuses on coupled fluid flow-solid deformation in rocks considering the effects of internal erosion induced by chemical reaction. In nature, many rocks are inherently anisotropic. The most prevalent type of anisotropy in rocks is transverse isotropy arising from a laminated microstructure. For such rocks, the mechanical response of the solid skeleton, the constitutive law of pore fluid flow, and their variation under the impact of internal erosion should follow the symmetry requirement of material transverse isotropy [32, 33, 84, 86, 87]. In terms of material compositions, natural rocks are usually heterogeneous and are made up of various constituents, including chemically stable minerals like quartz, and constituents that are prone to dissolve in acidic environment such as carbonate and feldspar [3, 8, 41, 57, 66, 71]. Taking carbon geological sequestration as an example, the increase of acidity of the reservoir fluid caused by CO<sub>2</sub> injection would substantially amplify the dissolution rate of carbonate minerals [11, 19, 25, 36, 57] and trigger mineral alteration in aluminosilicate minerals [2, 25].

The transition state theory is usually adopted to characterize the rate of chemical reaction that leads to solid erosion in natural rocks [53]. The theory indicates that the dissolution rate of the solid grains is proportional to the area of the surface between the interacting solid and fluid phases. The solid-fluid interaction in rocks generally takes place in open microcracks. Therefore, the reaction area that controls the solid dissolution rate would be proportional to the density of open microcracks, which can further be associated with the volumetric strain in the rock specimen [31]. To be more specific, dilative volumetric strain normally increases the density of open microcracks, while compressive strain reduces the opening of the cracks, leading to a decrease of the density of open microcracks. To consider the influence of mechanical deformation on the rate of chemical reaction, we introduce a phenomenological expression for the rate of solid dissolution that asymptotically reaches a constant maximum value at increasing dilative volumetric strain.

The loss of solid phases induced by chemical reactions would influence both the mechanical responses of the solid skeleton of the rocks and the behaviors of the pore fluid flow. For the impact on the mechanical properties, we introduce a damage model where the decrease of the elastic moduli of the solid skeleton is driven by the amount of dissolved solid. The impact of solid dissolution on pore fluid flow involves two competing aspects. On the one hand, solid dissolution enlarges the pores and facilitates pore fluid flow [28, 45]. We express the intrinsic permeability tensor as a function of porosity with a power-law approximation of the Kozeny-Carman equation [15, 37, 40, 73] with distinct parameters for permeability components along bed-normal and bed-parallel directions. On the other hand, since the dissolved solid and the fluid phase together form a thick fluid that permeates through the pore network, the increase of dissolved solid would result in higher viscosity of the thick fluid, which would impede the pore fluid flow [23, 51]. As a result, the two competing effects including the increased intrinsic permeability and fluid viscosity resulting from solid dissolution together determine the manifested behavior of pore fluid flow.

The novelty of this paper is summarized as follows. We develop a continuum framework for solid-fluid interaction in transversely isotropic rocks considering the impact of chemical reaction-induced solid dissolution based on the work of the Stanford group [82]. A phenomenological expression associating the rate of solid dissolution with the volumetric strain in the rock specimen is proposed to reflect the impact of mechanical deformation on the rate of chemical reactions in rocks. A damage model for elastic moduli is adopted for solid deformation, and the impact of solid dissolution on the intrinsic permeability as well as the viscosity of fluid is properly quantified in the framework. By treating the mixture of the fluid phase and the dissolved solid phase as a thick fluid, the framework follows the standard u/p formulation and can be solved with a standard mixed finite element scheme.

The order of the presentation in this paper is as follows. First we introduce the kinematics and conservation equations governing the solid-fluid interaction with internal erosion. Then, we introduce the constitutive theories for both the solid skeleton and the thick fluid with an emphasis on the impacts of solid dissolution. Thereafter, we discuss the mixed finite element formulation with a standard u/p formulation to derive the numerical solutions of the proposed framework. Lastly, we conduct three numerical examples to demonstrate the effects of chemical reaction-induced internal erosion on the solid-fluid interaction in transversely isotropic rocks in different subsurface systems. As for general notations and symbols, we denote symmetric identity tensors of ranks 2 and 4 by the symbols 1 and,  $\mathbb{I}$  respectively. Dot product and inner product are defined with symbols  $\cdot$  and : respectively. Tensorial operators  $\otimes$ ,  $\oplus$  and  $\ominus$  are defined such that  $(A \otimes B)_{ijkl} = A_{ij}B_{kl}$ ,  $(A \oplus B)_{ijkl} = A_{jl}B_{ik}$  and  $(A \ominus B)_{ijkl} = A_{il}B_{jk}$ .

## 2 Theory

We consider a mixture of solid and fluid in which the solid mass is decreasing due to erosion at a rate of  $\dot{m}_s$  per unit total volume of the mixture. We assume that the solid may be represented by residual and eroded parts with volume fractions  $\phi^{sr}$  and  $\phi^{se}$ , respectively, and the fluid has a volume fraction of  $\phi^f$ .

The closure condition on the volume fractions is given by

$$\phi^{sr} + \phi^{se} + \phi^f = 1. \tag{1}$$

We let  $\rho_{sr}$ ,  $\rho_{se}$ , and  $\rho_f$  denote the intrinsic mass densities of the residual solid, eroded solid, and fluid, respectively. The total mass density of the mixture is given by

$$\rho = \phi^{sr} \rho_{sr} + \phi^{se} \rho_{se} + \phi^f \rho_f. \tag{2}$$

We note that  $\rho_{sr}$  may not necessarily be equal to  $\rho_{se}$  since the pressures in these two materials are different.

Chemical erosion or weathering typically produces fine-grained sediments such as clay and silt, which can mix with the pure fluid to form a thick fluid resembling chocolate milk [30]. Focusing on this type of erosion, the volume fraction occupied by the eroded solid and pure fluid may be expressed as

$$\widetilde{\phi}^f = \phi^{se} + \phi^f \tag{3}$$

and its overall mass density as

$$\widetilde{\rho}_f = \frac{\phi^{se} \rho_{se} + \phi^f \rho_f}{\widetilde{\phi}^f} = \psi^{se} \rho_{se} + \psi^f \rho_f , \qquad (4)$$

where

$$\psi^{se} = \phi^{se}/\widetilde{\phi}^f$$
 and  $\psi^f = \phi^f/\widetilde{\phi}^f$  (5)

are the pore fractions occupied by the eroded solid and pure fluid, respectively. The pore fractions satisfy the closure condition

$$\psi^{se} + \psi^f = 1. ag{6}$$

Thus, the total mixture may be considered as consisting of residual solid and thick fluid whose total mass density is given by

$$\rho = \phi^{sr} \rho_{sr} + \widetilde{\phi}^f \widetilde{\rho}_f \,. \tag{7}$$

Note that  $\widetilde{\rho}_f$  varies with the concentration of the eroded solid.

#### 2.1 Balance of mass

The mass balance for the residual solid is given by the equation

$$\frac{d(\phi^{sr}\rho_{sr})}{dt} + \phi^{sr}\rho_{sr}\nabla \cdot \boldsymbol{v} = -\dot{m}^{s},\tag{8}$$

where v is the velocity of the residual solid,  $\dot{m}^s \geq 0$  is the rate of mass transfer from the residual solid to the surrounding fluid, and  $d(\cdot)/dt$  is the material time-derivative following the motion of the residual solid.

Coarse-grained particles such as sand and gravel will generally exhibit a settling velocity relative to the moving fluid, but Stokes law suggests that this relative velocity diminishes significantly with decreasing particle sizes. For very fine particles such as clay, the settling velocity may be neglected and the eroded solid may be assumed to follow the motion of the fluid. In this case, the mass balance equations for the fluid and eroded solid take the form

$$\frac{d^f(\phi^f \rho_f)}{dt} + \phi^f \rho_f \nabla \cdot \boldsymbol{v}_f = 0, \tag{9a}$$

$$\frac{d^f(\phi^{se}\rho_{se})}{dt} + \phi^{se}\rho_{se}\nabla \cdot \boldsymbol{v}_f = \dot{m}^s, \tag{9b}$$

where  $d^f(\cdot)/dt$  is the material time derivative following the motion of the fluid and  $v_f$  is the velocity of the fluid.

It is convenient to express the mass balance equations for the fluid following the motion of the residual solid. The transformation equation is given by

$$\frac{d^f(\cdot)}{dt} = \frac{d(\cdot)}{dt} + \boldsymbol{\nabla}(\cdot) \cdot \tilde{\boldsymbol{v}}_f, \qquad (10)$$

where  $\tilde{\boldsymbol{v}}_f = \boldsymbol{v}_f - \boldsymbol{v}$  is the relative velocity of the fluid with respect to the residual solid.

Furthermore, for barotropic flow the intrinsic pressure  $p_{\alpha}$  is related to the intrinsic mass density  $\rho_{\alpha}$  in phase  $\alpha$  (= sr, se, f) through the functional relation

$$p_{\alpha} = p_{\alpha}(\rho_{\alpha}), \qquad (11)$$

so that

$$\frac{d^{\alpha}p_{\alpha}}{dt} = p_{\alpha}'(\rho_{\alpha})\frac{d^{\alpha}\rho_{\alpha}}{dt}.$$
 (12)

But  $\rho_{\alpha} = M_{\alpha}/V_{\alpha}$ . Differentiating yields

$$\frac{1}{\rho_{\alpha}} \frac{d^{\alpha} \rho_{\alpha}}{dt} = \dot{\vartheta}_{\alpha} - \frac{1}{V_{\alpha}} \frac{d^{\alpha} V_{\alpha}}{dt} \,, \tag{13}$$

where

$$\dot{\vartheta}_{\alpha} = \frac{1}{\rho_{\alpha} V_{\alpha}} \frac{d^{\alpha} M_{\alpha}}{dt} = \begin{cases} -\dot{m}_{s} / \rho_{\alpha} \phi^{\alpha} & \alpha = sr \\ \dot{m}_{s} / \rho_{\alpha} \phi^{\alpha} & \alpha = se \\ 0 & \alpha = f \end{cases}$$
(14)

is the volumetric strain rate in  $V_{\alpha}$  resulting from mass exchanges (equal to zero for the pure fluid).

Substituting equation (13) into equation (12) yields

$$-\frac{d^{\alpha}p_{\alpha}}{dt} = \rho_{\alpha}p'(\rho_{\alpha})\left(\frac{1}{V_{\alpha}}\frac{d^{\alpha}V_{\alpha}}{dt} - \dot{\vartheta}_{\alpha}\right). \tag{15}$$

The quantity inside the parentheses is the intrinsic net volumetric strain in  $V_{\alpha}$  accounting for mass exchanges, from which we identify

$$K_{\alpha} = \rho_{\alpha} p_{\alpha}'(\rho_{\alpha}) \tag{16}$$

as the intrinsic bulk modulus of phase  $\alpha$ . Thus,

$$\frac{d\rho_{\alpha}}{dt} = \frac{\rho_{\alpha}}{K_{\alpha}} \frac{dp_{\alpha}}{dt} \,, \tag{17}$$

and so the mass balance equations can be written in the alternative forms

$$\frac{d\phi^{sr}}{dt} + \frac{\phi^{sr}}{K_{sr}} \frac{dp_{sr}}{dt} + \phi^{sr} \nabla \cdot \boldsymbol{v} = -\frac{\dot{m}^s}{\rho_{sr}}, \qquad (18a)$$

$$\frac{d\phi^f}{dt} + \frac{\phi^f}{K_f} \frac{dp}{dt} + \phi^f \nabla \cdot \boldsymbol{v} = -\nabla \cdot (\phi^f \widetilde{\boldsymbol{v}}_f) - \frac{1}{K_f} \nabla p \cdot (\phi^f \widetilde{\boldsymbol{v}}_f), \qquad (18b)$$

$$\frac{d\phi^{se}}{dt} + \frac{\phi^{se}}{K_{se}} \frac{dp}{dt} + \phi^{se} \nabla \cdot \boldsymbol{v} = -\nabla \cdot (\phi^{se} \widetilde{\boldsymbol{v}}_f) 
- \frac{1}{K_{se}} \nabla p \cdot (\phi^{se} \widetilde{\boldsymbol{v}}_f) + \frac{\dot{m}^s}{\rho_{se}}.$$
(18c)

In these last two equations, we have assumed that  $p_f = p_{se} \equiv p$ , which is true if the eroded solid is in a state of suspension within the volume of the pure fluid.

The mass balance equation for the thick fluid can be obtained by adding equations (18b) and (18c):

$$\frac{d\widetilde{\phi}^f}{dt} + \left(\frac{\phi^f}{K_f} + \frac{\phi^{se}}{K_{se}}\right) \frac{dp}{dt} + \widetilde{\phi}^f \nabla \cdot \boldsymbol{v} 
= -\nabla \cdot \boldsymbol{q} - \left(\frac{\psi^f}{K_f} + \frac{\psi^{se}}{K_{se}}\right) \nabla p \cdot \boldsymbol{q} + \frac{\dot{m}^s}{\rho_{se}},$$
(19)

where

$$\mathbf{q} = \widetilde{\phi}^f \widetilde{\mathbf{v}}_f. \tag{20}$$

is the superficial (Darcy) velocity [4, 5, 17, 67, 83].

## 2.2 Balance of linear momentum

Adopting once again the three-phase description of the solid-fluid mixture, we write the linear momentum balance as

$$\nabla \cdot \boldsymbol{\sigma}^{sr} + \boldsymbol{\pi}^{sr} + \phi^{sr} \rho_{sr} \boldsymbol{g} = \phi^{sr} \rho_{sr} \boldsymbol{a} - \dot{m}^{s} \boldsymbol{v}, \qquad (21a)$$

$$\nabla \cdot \boldsymbol{\sigma}^f + \boldsymbol{\pi}^f + \phi^f \rho_f \boldsymbol{g} = \phi^f \rho_f \boldsymbol{a}_f, \qquad (21b)$$

$$\nabla \cdot \boldsymbol{\sigma}^{se} + \boldsymbol{\pi}^{se} + \phi^{se} \rho_{se} \boldsymbol{g} = \phi^{se} \rho_{se} \boldsymbol{a}_f + \dot{m}^s \boldsymbol{v}_f, \qquad (21c)$$

where  $\sigma^{\alpha}$  is the partial Cauchy stress tensor for phase  $\alpha$ ,  $\pi^{\alpha}$  is the body force exerted on phase  $\alpha$  by the other two phases, g is the gravity acceleration

vector,  $\boldsymbol{a}$  is the material acceleration of the residual solid, and  $\boldsymbol{a}_f$  is the material acceleration of the fluid and eroded solid. The body forces  $\boldsymbol{\pi}$  satisfy the closure condition

$$\boldsymbol{\pi}^{sr} + \boldsymbol{\pi}^f + \boldsymbol{\pi}^{se} = \mathbf{0} \,. \tag{22}$$

Adding all three linear momentum equations yields

$$\nabla \cdot \boldsymbol{\sigma} + \rho \boldsymbol{g} = \phi^{sr} \rho_{sr} \boldsymbol{a} + \widetilde{\phi}^f \widetilde{\rho}_f \boldsymbol{a}_f + \boldsymbol{f}, \tag{23}$$

where  $\sigma = \sigma^{sr} + \sigma^{se} + \sigma^{f}$  is the total Cauchy stress tensor and

$$f = \dot{m}^s (v_f - v) \equiv \frac{\dot{m}^s}{\widetilde{\phi}^f} q$$
 (24)

is the equivalent inertia force arising from the mass transfer term. The term f is typically small, whereas the acceleration terms may be ignored in the quasi-static regime.

We can add the last two lines of equation (21) and write the result in the alternative form

$$\nabla \cdot \widetilde{\boldsymbol{\sigma}}^f + \widetilde{\boldsymbol{\pi}}^f + \widetilde{\boldsymbol{\phi}}^f \widetilde{\boldsymbol{\rho}}_f \boldsymbol{g} = \widetilde{\boldsymbol{\phi}}^f \widetilde{\boldsymbol{\rho}}_f \boldsymbol{a}_f + \dot{m}^s \boldsymbol{v}_f. \tag{25}$$

Because the fluid and eroded solid are assumed to move as one body, we can view the system as a mixture of eroded solid and thick fluid exchanging masses with each other. We note that  $\sigma^{se}$  and  $\sigma^{f}$  are both isotropic tensors in the present formulation.

#### 2.3 Thermodynamics

Having idealized the system as a mixture of residual solid and thick fluid, we now use the first and second laws of thermodynamics to identify the effective stress and energy-conjugate pairs. From the first law, we write the following expression for the rate of change of internal energy for a mixture of solid and fluid exchanging mass at the rate of  $\dot{m}_s$  per unit total volume:

$$\rho \dot{e} = \boldsymbol{\sigma}^{sr} : \boldsymbol{d} + \widetilde{\boldsymbol{\sigma}}^{f} : \boldsymbol{d}_{f} + \frac{1}{2} \dot{m}_{s} (\|\boldsymbol{v}_{f}\|^{2} - \|\boldsymbol{v}\|^{2}), \qquad (26)$$

where  $\dot{e}$  is the rate of change of internal energy per unit total mass, and d and  $d_f$  are the rate of deformation tensors for the residual solid and thick fluid, respectively. In this equation, we have omitted the non-mechanical powers produced by the heat supply and heat flux. Recognizing that  $\tilde{\sigma}^f$  is an isotropic tensor, we write the rate of change of internal energy in terms of the total Cauchy stress tensor  $\sigma$  as

$$\rho \dot{e} = \boldsymbol{\sigma} : \boldsymbol{d} - p \widetilde{\phi}^f \boldsymbol{\nabla} \cdot \widetilde{\boldsymbol{v}}_f + \frac{1}{2} \dot{m}_s (\|\boldsymbol{v}_f\|^2 - \|\boldsymbol{v}\|^2).$$
 (27)

8

We now use the developments presented in Zhao and Borja [82] to develop an expression for the effective Cauchy stress tensor incorporating the compressibility of the solid phase. To this end, we assume that the Cauchy effective stress tensor  $\sigma'$  satisfies the elastic-damage constitutive equation [60, 61, 70]

$$\sigma' = (1 - D_e)\mathbb{C}^e : \epsilon \,, \tag{28}$$

where  $\mathbb{C}^e$  is the elastic moduli tensor (which can be anisotropic),  $\epsilon$  is the small-strain tensor (assumed fully elastic), and  $D_e$  represents damage due to erosion that can take on values from zero (no erosion) to one (complete erosion). The rate of change of internal energy then takes the alternative form

$$\rho \dot{e} = \boldsymbol{\sigma}' : \boldsymbol{d} + \theta \dot{p} + \boldsymbol{\chi} \cdot \tilde{\boldsymbol{v}}_f + \frac{1}{2} \dot{m}_s (\|\boldsymbol{v}_f\|^2 - \|\boldsymbol{v}\|^2) + \dot{m}^s p \left(\frac{1}{\rho_{sr}} - \frac{1}{\rho_{se}}\right),$$
(29)

where

$$\boldsymbol{\sigma}' = \boldsymbol{\sigma} + p\boldsymbol{b} \tag{30}$$

is the effective stress tensor,

$$\boldsymbol{b} = \mathbf{1} - (1 - D_e) \frac{\mathbf{1} : \mathbb{C}^e}{3K_{sr}} \tag{31}$$

is the Biot tensor,

$$\theta = \left(\frac{\beta}{K_{sr}} + \frac{\phi^f}{K_f} + \frac{\phi^{se}}{K_{se}}\right) p, \qquad (32)$$

$$\chi = \left[ \left( \frac{\phi^f}{K_f} + \frac{\phi^{se}}{K_{se}} \right) \nabla p + \nabla \widetilde{\phi}^f \right] p, \qquad (33)$$

and

$$\beta = \frac{1}{3}\mathbf{1} : \mathbf{b} - \widetilde{\phi}^f. \tag{34}$$

The above development follows the same line as the classic flow and deformation in anisotropic media with mass exchanges taking place between the solid and fluid.

For purposes of developing constitutive models, the second law, or entropy inequality, must be satisfied. To this end, we assume the following Helmholtz free energy density function that is quadratic in the strains (again, neglecting plasticity), of the form

$$\Psi = \frac{1}{2}(1 - D_e)\boldsymbol{\epsilon} : \mathbb{C}^e : \boldsymbol{\epsilon} + \Psi^q(p, \widetilde{\boldsymbol{u}}_f), \qquad (35)$$

where  $\tilde{u}_f = u_f - u$  is the relative displacement of the thick fluid with respect to the residual solid. The Clausius-Duhem inequality then leads to the local dissipation condition [6]

$$\mathcal{D} = \rho \dot{e} - \dot{\Psi} > 0, \tag{36}$$

or

$$\mathcal{D} = \boldsymbol{\sigma}' : \boldsymbol{d} + \theta \dot{p} + \boldsymbol{\chi} \cdot \widetilde{\boldsymbol{v}}_f + \frac{1}{2} \dot{m}_s (\|\boldsymbol{v}_f\|^2 - \|\boldsymbol{v}\|^2) + \dot{m}^s p \left(\frac{1}{\rho_{sr}} - \frac{1}{\rho_{se}}\right) - \dot{\Psi} \ge 0.$$
(37)

Imposing the Coleman-Noll [48] relations yields

$$\sigma' = (1 - D_e)\mathbb{C}^e : \epsilon, \qquad \theta = \frac{\partial \Psi^q}{\partial p}, \qquad \chi = \frac{\partial \Psi^q}{\partial \tilde{u}_f},$$
 (38)

and the reduced dissipation inequality

$$\mathcal{D} = \frac{1}{2}\dot{m}_s(\|\mathbf{v}_f\|^2 - \|\mathbf{v}\|^2) + \dot{m}^s p\left(\frac{1}{\rho_{sr}} - \frac{1}{\rho_{se}}\right) \ge 0.$$
 (39)

Note that  $(38)_1$  is the same as (28). Now, assuming  $\rho_{sr} = \rho_{se}$  and noting that  $\dot{m}_s \geq 0$ , the reduced dissipation inequality is satisfied when  $\|\boldsymbol{v}_f\| \geq \|\boldsymbol{v}\|$ , or when the thick fluid is moving *faster* than the residual solid. Interestingly, this condition for dissipation is similar to the one developed for double-porosity media where fluids in the macropores are required to move faster than the fluids in the micropores, see Borja and Choo [7].

#### 2.4 Constitutive theory

Internal erosion leads to increased porosity, causing the solid to degrade its resisting capacity. The process is similar to mechanical damage in that the effective area created by the loss of solid mass is decreased. There is evidence that in some rocks, the pore spaces created by solid dissolution due to  $CO_2$  exposure, for example, are randomly distributed [47].

For a transversely isotropic material, the elastic moduli tensor can be expressed in terms of five constants as follows

$$\mathbb{C}^{e} = \lambda \mathbf{1} \otimes \mathbf{1} + 2\mu_{T} \mathbb{I} + a(\mathbf{1} \otimes \boldsymbol{m} + \boldsymbol{m} \otimes \mathbf{1}) + b\boldsymbol{m} \otimes \boldsymbol{m} + (\mu_{L} - \mu_{T})(\mathbf{1} \oplus \boldsymbol{m} + \boldsymbol{m} \oplus \mathbf{1} + \mathbf{1} \ominus \boldsymbol{m} + \boldsymbol{m} \ominus \mathbf{1}),$$
(40)

where  $\lambda$ ,  $\mu_T$ ,  $\mu_L$ , a, and b are the elastic constants [68], and

$$m = n \otimes n \tag{41}$$

is the microstructure tensor defining the orientation of the plane of isotropy, and n is the normal vector of the bedding plane. Alternatively, the elastic constants may be replaced with more physically meaningful quantities such as  $E_1$ ,  $E_2$ ,  $\nu_{12}$ ,  $\nu_{23}$ , and  $G_{12}$ , where  $E_1$  is the Young's modulus perpendicular

to the plane of isotropy;  $E_2$  is the Young's modulus on the plane of isotropy;  $\nu_{12}$  and  $\nu_{23}$  are Poisson's ratios; and  $G_{12}$  is the shear modulus [20, 62].

Next, we quantify the evolution of the damage variable  $D_e$ . For a representative elementary volume (REV) where the pore spaces are statistically distributed, the area fraction and volume fraction are equivalent [9], so the evolution of  $D_e$  may be expressed as

$$\dot{D}_e = \frac{\dot{m}^s}{\rho_{sr}} \,. \tag{42}$$

We remark that the free energy may be enhanced to account for combined mechanical and erosion-induced damage, but we shall not consider the mechanical damage in this work and focus on damage due to erosion.

The constitutive law for the rate of erosion depends on the physical mechanisms of the erosion process. For suffusion type of erosion in soil mechanics, the rate at which the finer particles are removed and transported depends on the hydraulic gradient and grain size distribution [46, 64]. In this work, we shall focus on chemical dissolution as the relevant type of erosion. In this case, the rate of erosion is expressed in terms of the rate of mass lost per unit volume of the residual solid,  $\dot{\mu}_{sr}$ , i.e.,

$$\dot{m}^s = \dot{\mu}_{sr} \phi^{sr} \,, \tag{43}$$

where  $\phi^{sr}$  is the volume fraction of the residual solid.

Transition state theory [38, 39, 53] states that the rate of dissolution of a mineral varies with the surface area of the mineral exposed to chemical reaction [75, 76]. This suggests that the rate of dissolution may be assumed to be proportional to the microcrack density, since the higher the microcrack density, the more surface area would be exposed to chemical reaction. Experimental observations from extension tests on clay [69] suggest that the microcrack density varies with the dilative volumetric strain in an exponential fashion, increasing asymptotically to a constant value at infinite volumetric strain. Thus, the constitutive law for  $\dot{\mu}_{sr}$  may be expressed as an exponential function of the volumetric strain as follows

$$\dot{\mu}_{sr} = B - (B - C)e^{-A\varepsilon_v}, \tag{44}$$

where A, B, and C are nonnegative fitting parameters. Since porous materials are already "damaged" even before they are stretched, the fitting parameter C, representing the rate of dissolution at zero volumetric strain, must have a nonnegative value. Furthermore, the parameter B>C represents the limiting rate of dissolution at infinite volumetric strain. The parameter A>0 determines the shape of the curve delineating the variation of microcrack density with volumetric strain, and may be determined from extension tests such as those conducted by Spyropoulos et al. [69]. Further discussions on this development may be found in Borja et al. [10].

As for fluid flow, we adopt Darcy's law, which states that

$$\boldsymbol{q} = -\frac{\kappa}{\mu} \cdot (\boldsymbol{\nabla} p - \widetilde{\rho}_f \boldsymbol{g}), \qquad (45)$$

where  $\kappa$  is the intrinsic permeability tensor of the residual solid,  $\mu$  is the viscosity of the thick fluid, g is the gravity acceleration constant, and z is the elevation potential. The ratio  $\mathbf{k} = \kappa/\mu$  is known as the hydraulic conductivity (or simply, permeability) of the system. For a transversely isotropic material, the intrinsic permeability tensor can be expressed as [55, 77, 79, 80]

$$\kappa = \kappa_{\perp} m + \kappa_{\parallel} (1 - m), \qquad (46)$$

where  $\kappa_{\perp}$  and  $\kappa_{\parallel}$  are the components normal to and along the plane of isotropy, respectively, and m is the microstructure tensor defined in equation (41).

Solid dissolution results in competing effects on the hydraulic conductivity in that the pore space increase in the solid results in a higher intrinsic permeability (assuming the pore spaces are interconnected), but the thickening of the fluid due to the addition of dissolved solid also increases the overall viscosity of the fluid. To better quantify the overall effect on the hydraulic conductivity, we adopt a conventional power-law relationship [14, 27, 85] to relate the coefficients of the intrinsic permeability to the porosity of the material:

$$\kappa_{\perp} \propto \kappa_{\perp 0} \left( \frac{\widetilde{\phi}^f}{\widetilde{\phi}_0^f} \right)^{n_{\perp}}, \qquad \kappa_{\parallel} \propto \kappa_{\parallel 0} \left( \frac{\widetilde{\phi}^f}{\widetilde{\phi}_0^f} \right)^{n_{\parallel}}.$$
(47)

Note that  $\widetilde{\phi}_0^f$  is the initial porosity while  $\widetilde{\phi}^f$  is the porosity that evolves with solid dissolution; and  $n_{\parallel}$  and  $n_{\perp}$  are the exponential parameters in the power-law relationships. In this work, we assume  $n_{\parallel} = n_{\perp} = 3$ .

For dynamic viscosity  $\mu$ , we consider the work of Coussot [16], who estimated  $\mu$  for a mixture of water and suspended solids as

$$\mu = \mu_w \left( 1 + \frac{0.75\psi^{se}}{0.605 - \psi^{se}} \right)^2, \tag{48}$$

where  $\mu_w$  is the viscosity of water and  $\psi^{se}$  is the concentration of eroded solid. We see that the dynamic viscosity varies nonlinearly with the concentration  $\psi^{se}$ . This expression for viscosity is valid for very concentrated solutions, up to  $\psi^{se} = 0.55$  [16].

In view of equations (47) and (48), we derive

$$\frac{\kappa}{\mu} = \alpha \frac{\kappa_0}{\mu_0},\tag{49}$$

where  $\alpha$  is defined as the ratio

$$\alpha = \left(\frac{1}{1 - \eta/s^e}\right)^3 / \left(1 + \frac{0.75\psi^{se}}{0.605 - \eta/s^e}\right)^2. \tag{50}$$

The variation of  $\alpha$  with  $\psi^{se}$  is shown in Figure 1. We observe that as  $\psi^{se}$  increases,  $\alpha$  increases first and then decreases. This means that at the initial

stage of erosion, the flow is first enhanced by the increase in intrinsic permeability, but as the viscosity of the thick fluid increases with more and more solid being dissolved, fluid flow becomes more difficult and the flow diminishes.

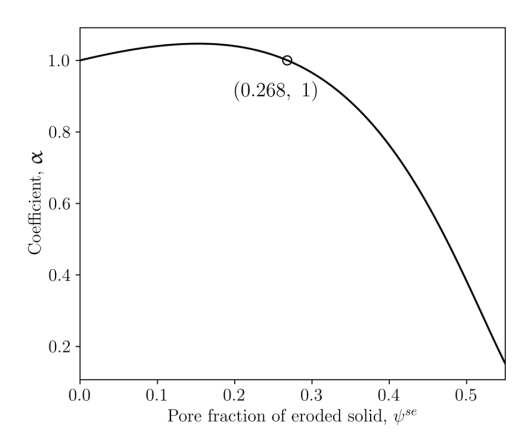


**Fig. 1.** Variation of  $\alpha$  with solid concentration in the thick fluid.

## 3 Finite element formulation

We employ the classic u/p formulation for solid-fluid interaction with internal erosion. The two relevant conservation equations are the balance of linear momentum and the balance of mass for the whole mixture. Assuming quasistatic loading, the balance of linear momentum is derived from equation (23) by omitting the acceleration terms and expressing the body force f in terms of Darcy flux q as follows,

$$\nabla \cdot (\boldsymbol{\sigma}' - p\boldsymbol{b}) - \frac{\dot{m}^s}{\widetilde{\phi}^f} \boldsymbol{q} + \rho \boldsymbol{g} = \boldsymbol{0}.$$
 (51)

The balance of mass is derived by adding equations (18a) and (19) and using the developments in Zhao and Borja [82] to obtain

$$\frac{1}{\mathcal{M}} \frac{dp}{dt} + \mathbf{b} : \dot{\boldsymbol{\epsilon}} + \boldsymbol{\nabla} \cdot \boldsymbol{q} + \left(\frac{\psi^f}{K_f} + \frac{\psi^{se}}{K_{se}}\right) \boldsymbol{\nabla} p \cdot \boldsymbol{q} + \left(\frac{1}{\rho_{sr}} - \frac{1}{\rho_{se}}\right) \dot{m}^s = 0,$$
(52)

where

$$\frac{1}{\mathcal{M}} = \frac{\beta}{K_{sr}} + \frac{\phi^f}{K_f} + \frac{\phi^{se}}{K_{se}}.$$
 (53)

We note that both  $\sigma'$  and  $\dot{m}_s$  can be expressed in terms of u through the elastic and dissolution constitutive laws, whereas q can be expressed in terms of p through Darcy's law. Hence, we recover the u/p formulation in which u and p are the independent variables.

We now consider a closed domain  $\bar{\mathcal{B}}$  denoted as  $\bar{\mathcal{B}} = \mathcal{B} \cup \partial \mathcal{B}$ , where  $\mathcal{B}$  is the open domain and  $\partial \mathcal{B}$  is its boundary. The boundary  $\partial \mathcal{B}$  is decomposed into  $\partial \mathcal{B}_u$  and  $\partial \mathcal{B}_t$  where the displacement and traction boundary conditions are prescribed; and into  $\partial \mathcal{B}_p$  and  $\partial \mathcal{B}_q$  where the pressure and flux boundary conditions are satisfied. The following set relations hold:

$$\overline{\partial \mathcal{B}_u \cup \partial \mathcal{B}_t} = \overline{\partial \mathcal{B}_n \cup \partial \mathcal{B}_g} = \partial \mathcal{B}, \qquad (54a)$$

$$\partial \mathcal{B}_u \cap \partial \mathcal{B}_t = \partial \mathcal{B}_n \cap \partial \mathcal{B}_q = \varnothing \,, \tag{54b}$$

where  $\emptyset$  is the null set and the overlines denote a closure. The strong form (S) of the problem is now stated as follows: Find  $\boldsymbol{u}$  and p such that equations (51) and (52) are satisfied in  $\mathcal{B}$ , subject to the boundary conditions

$$\mathbf{u} = \hat{\mathbf{u}} \text{ on } \partial \mathcal{B}_u \,, \tag{55a}$$

$$\mathbf{n} \cdot \mathbf{\sigma} = \hat{\mathbf{t}} \text{ on } \partial \mathcal{B}_t,$$
 (55b)

$$p = \hat{p} \text{ on } \partial \mathcal{B}_p,$$
 (55c)

$$-\mathbf{n} \cdot \mathbf{q} = \hat{q} \text{ on } \partial \mathcal{B}_q. \tag{55d}$$

and the initial conditions

$$u(x, t = 0) = u_0(x), \ p(x, t = 0) = p_0(x).$$
 (56)

To develop the weak form (W), we define sets of trial functions

$$S_u = \{ \boldsymbol{u} | \boldsymbol{u} \in H^1, \boldsymbol{u} = \hat{\boldsymbol{u}} \text{ on } \partial B_u \},$$
 (57a)

$$S_p = \{ p | p \in H^1, p = \hat{p} \text{ on } \partial \mathcal{B}_p \},$$
 (57b)

and sets of weighting functions

$$\mathcal{V}_u = \{ \boldsymbol{\eta} | \boldsymbol{\eta} \in H^1, \boldsymbol{\eta} = \mathbf{0} \text{ on } \partial \mathcal{B}_u \},$$
 (58a)

$$\mathcal{V}_p = \{ \varphi | \varphi \in H^1, \varphi = 0 \text{ on } \partial \mathcal{B}_p \}.$$
 (58b)

The weak form (W) is then stated as follows: Find  $\{u, p\} \in \mathcal{S}_u \times \mathcal{S}_p$  such that for all  $\{\eta, \varphi\} \in \mathcal{V}_u \times \mathcal{V}_p$ ,

$$\int_{\mathcal{B}} \nabla \boldsymbol{\eta} : \boldsymbol{\sigma} \, dV + \int_{\mathcal{B}} \nabla \boldsymbol{\eta} \cdot \frac{\dot{m}^s}{\widetilde{\phi}^f} \boldsymbol{q} \, dV - \int_{\mathcal{B}} \rho \boldsymbol{g} \cdot \boldsymbol{\eta} \, dV = \int_{\partial \mathcal{B}_t} \hat{\boldsymbol{t}} \cdot \boldsymbol{\eta} \, dV \,, \quad (59a)$$

$$\int_{\mathcal{B}} \left[ \frac{1}{\mathcal{M}} \dot{p} + \boldsymbol{b} : \dot{\boldsymbol{\epsilon}} + \left( \frac{\psi^f}{K_f} + \frac{\psi^{se}}{K_{se}} \right) \boldsymbol{\nabla} p \cdot \boldsymbol{q} + \left( \frac{1}{\rho_{sr}} - \frac{1}{\rho_{se}} \right) \dot{m}^s \right] \varphi \, dV$$

$$= \int_{\mathcal{B}} \boldsymbol{\nabla} \varphi \cdot \boldsymbol{q} \, dV + \int_{\partial \mathcal{B}_a} \varphi \hat{q} \, dA \, . \tag{59b}$$

For brevity in notation, the quantity  $(\cdot)$  at time step  $t_n$  is denoted as  $(\cdot)_n$ , while the quantities without any subscript are evaluated at time step  $t_{n+1}$ .

A mixed finite element method similar to those used in multiphysics problems can be used for the current problem. Let  $\mathbf{N}_u$  denote the shape function matrix for the displacement field and  $\mathbf{B}$  as the strain-displacement transformation matrix. Similarly, let  $\mathbf{N}_p$  denote the shape function matrix for the pore pressure field and  $\mathbf{E}$  the matrix denoting its gradient. In the current formulation, we use the volume fraction at time  $t_n$  to march the solution in time (i.e., explicit), which is acceptable since the volume fractions do not change much. Therefore, the residual form of the weak form can be written as

$$\mathcal{R}_{\boldsymbol{u}} = \int_{\mathcal{B}} \mathcal{B}^{\mathsf{T}} \{ \boldsymbol{\sigma} \} dV + \int_{\mathcal{B}} \mathbf{N}_{\boldsymbol{u}}^{\mathsf{T}} \frac{\dot{m}^{s}}{\widetilde{\phi}_{n}^{f}} \boldsymbol{q} dV - \int_{\mathcal{B}} \mathbf{N}_{u}^{\mathsf{T}} \hat{\boldsymbol{t}} dA,$$

$$(60)$$

where  $\{\sigma\}$  is the Cauchy stress vector in Voigt form, and

$$\mathcal{R}_{p} = \int_{\mathcal{B}} \mathbf{N}_{p}^{\mathsf{T}} \left[ \frac{1}{\mathcal{M}_{n}} (p - p_{n}) + \boldsymbol{b} : (\boldsymbol{\epsilon} - \boldsymbol{\epsilon}_{n}) \right] dV 
+ \Delta t \int_{\mathcal{B}} \mathbf{N}_{p}^{\mathsf{T}} \left( \frac{\psi_{n}^{f}}{K_{f}} + \frac{\psi_{n}^{se}}{K_{se}} \right) \boldsymbol{\nabla} p \cdot \boldsymbol{q} \, dV 
+ \int_{\mathcal{B}} \mathbf{N}_{p}^{\mathsf{T}} \left( \frac{1}{\rho_{sr}} - \frac{1}{\rho_{se}} \right) \dot{m}^{s} dV - \int_{\mathcal{B}} \Delta t \mathbf{E}^{\mathsf{T}} \boldsymbol{q} \, dV 
- \int_{\partial \mathcal{B}_{q}} \Delta t \mathbf{N}_{p}^{\mathsf{T}} \boldsymbol{q} \, dA .$$
(61)

The residuals defined above are nonlinear with respect to the unknown vector of nodal displacements d and nodal pressures p. To solve for the unknown vectors, we employ Newton's method and write the linearized problem as

$$\left[\frac{\mathbf{K}_{11}|\mathbf{K}_{12}|}{\mathbf{K}_{21}|\mathbf{K}_{22}}\right] \left\{\frac{\delta \mathbf{d}}{\delta \mathbf{p}}\right\} = -\left\{\frac{\mathbf{R}_u}{\mathbf{R}_p}\right\},$$
(62)

where  $\delta d$ ,  $\delta p$  indicate incremental nodal displacements and nodal pressures respectively for one Newton iteration step. The tangent operator may be evaluated from the expressions summarized in Appendix A.

Using the developments presented in Zhao and Borja [82], the intrinsic pressure of the solid phase  $p_{sr}$  can be expressed as a function of the pore pressure p and the effective stress  $\sigma'$ . Thus, the mass balance equation of the solid phase (18a) can be expressed in the alternative form (see [82])

$$\frac{d\phi^{sr}}{dt} + \frac{\beta}{K_{sr}} \frac{dp}{dt} - \psi : \dot{\boldsymbol{\epsilon}} + \phi^{sr} \nabla \cdot \boldsymbol{v} = -\frac{\dot{m}^s}{\rho_{sr}}, \tag{63}$$

where

$$\psi = \frac{1:\mathbb{C}^e}{3K_{sr}}. (64)$$

This equation can be solved numerically for  $\phi^{sr}$  as

$$\phi_{n+1}^{sr} = \phi_n^{sr} - \frac{\beta_{n+1}}{K_{sr}} (p_{n+1} - p_n) + \psi : (\epsilon_{n+1} - \epsilon_n)$$

$$- \phi_{n+1}^{sr} (\epsilon_{v,n+1} - \epsilon_{v,n}) - \Delta t \frac{\dot{m}_{n+1}^s}{\rho_{sr}},$$

$$(65)$$

where

$$\beta_{n+1} = \frac{1}{3} \mathbf{1} : \mathbf{b} - 1 + \phi_{n+1}^{sr}, \quad \dot{m}_{n+1}^{s} = \phi_{n+1}^{sr} [B - (B - C)e^{-A\varepsilon_{v,n+1}}].$$
 (66)

Therefore, the volume fraction of solid can be calculated as

$$\phi_{n+1}^{sr} = a/b,\tag{67}$$

where

$$a = \phi_n^{sr} + \boldsymbol{\psi} : (\boldsymbol{\epsilon}_{n+1} - \boldsymbol{\epsilon}_n) - \frac{1}{K_{sr}} \left(\frac{1}{3}\mathbf{1} : \boldsymbol{b} - 1\right) (p_{n+1} - p_n)$$
 (68)

and

$$b = 1 + \varepsilon_{v,n+1} - \varepsilon_{v,n} + \frac{p_{n+1} - p_n}{K_{sr}} + \frac{B - (B - C)e^{-A\varepsilon_{v,n+1}}}{\rho_{sr}} \Delta t.$$
 (69)

The parameters associated with the volume fraction of solid needs to be updated as

$$\widetilde{\phi}^f = 1 - \phi^{sr}, \quad \kappa_{\perp} = \kappa_{\perp 0} \left( \frac{\widetilde{\phi}^f}{\widetilde{\phi}_0^f} \right)^{n_{\perp}}, \quad \kappa_{\parallel} = \kappa_{\parallel 0} \left( \frac{\widetilde{\phi}^f}{\widetilde{\phi}_0^f} \right)^{n_{\parallel}},$$
 (70a)

$$\beta = \frac{1}{3}\mathbf{1} : \boldsymbol{b} - \widetilde{\phi}^f, \quad \psi^f = \frac{\phi^f}{\widetilde{\delta}^f}, \quad \psi^{se} = 1 - \psi^f.$$
 (70b)

The iterative procedure from time step  $t_n$  to  $t_{n+1}$  is stated as follows

Step 1. Project solution,  $u_n$  and  $p_n$ , at time step  $t_n$  over the domain.

Step 2. Compute the parameters using  $u_n$  and  $p_n$ :

$$\widetilde{\phi}_n^f$$
,  $\phi_n^{sr}$ ,  $\beta_n$ ,  $\mathcal{M}_n$ ,  $\psi_n^f$ ,  $\psi_n^{se}$ ,  $\kappa_{\perp,n}$ ,  $\kappa_{\parallel,n}$  and  $\mu_n$ .

Step 3. Compute  $\boldsymbol{u}_{n+1}$  and  $p_{n+1}$  using  $\widetilde{\phi}_n^f$ ,  $\phi_n^{sr}$ ,  $\beta_n$ ,  $\mathcal{M}_n$ ,  $\psi_n^f$ ,  $\psi_n^{se}$ ,  $\kappa_{\perp,n}$ ,  $\kappa_{\parallel,n}$  and  $\mu_n$ .

## 4 Numerical examples

In this section, we present three numerical examples demonstrating the impact of internal erosion on the solid-fluid interaction in transversely isotropic porous rocks. For the first example, we study the 1D Terzaghi consolidation problem with internal erosion. Next, we consider the reactive fluid injection in a stratum of transversely isotropic porous rock. For the third and final example, we model and simulate the dissolution of calcarenite and fit the experimental results using our formulation. In all simulations, we employ equal-order (bilinear) interpolations on the displacement and pore pressure fields, with a polynomial pressure projection stabilization [74]. Furthermore, no softening or strain localization is involved in any of the simulations, so nonlocal stabilization schemes such as the gradient-enhanced [10] and phase-field approaches [34, 72] are not needed in any of the problems solved.

## 4.1 Benchmark problem: the Terzaghi 1D consolidation

The Terzaghi 1D consolidation [88] is commonly used as a benchmark solution for more complex problems. The setup consists of a column of fluid-saturated geologic material subjected to instantaneous compressive load on the top surface, which is held constant with time. The load generates an initially uniform excess pore pressure distribution, which dissipates with time at a rate that depends on the spatial distance of the point in the column from the top surface. As the excess pore pressure dissipates, the material compacts and the height of the column decreases. The process continues until all the excess pore pressures have dissipated.

In the present example, we add a certain variation to the Terzaghi problem and include internal erosion in the form of chemical dissolution. We assume that the initial porosity is uniform at 0.1, which results in a uniform initial rate of internal erosion. As the material consolidates and the column compacts, the pore spaces diminish and so does the rate of internal erosion. However, the degree of consolidation is not uniform across the height, and so the rate of internal erosion also varies spatially within the column.

For the layout, we consider a rectangular column 0.01 m wide and 0.1 m tall as depicted in Figure 2. The left, right, and bottom boundaries have no flux while the top surface serves as a drainage boundary. Because this is a one-dimensional problem, we prescribe the horizontal plane as the plane of isotropy and only consider flow and deformation in the (cross-anisotropic) vertical direction. The parameters used in the simulation were obtained from Zhao and Borja [82] for Tournemire shale and are tabulated in Table 1. The applied load is taken as  $\omega = 100$  MPa.

Figure 3a shows the evolution of porosity of the material. As expected, the porosity increases with depth at a given time instant. As the fluid is squeezed out near the drainage boundary, the pores are compressed and the rate of dissolution decreases. However, farther away from the drainage boundary, the

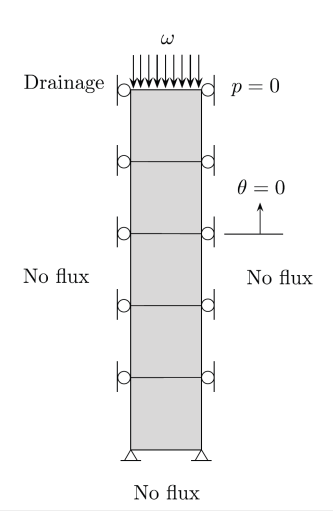


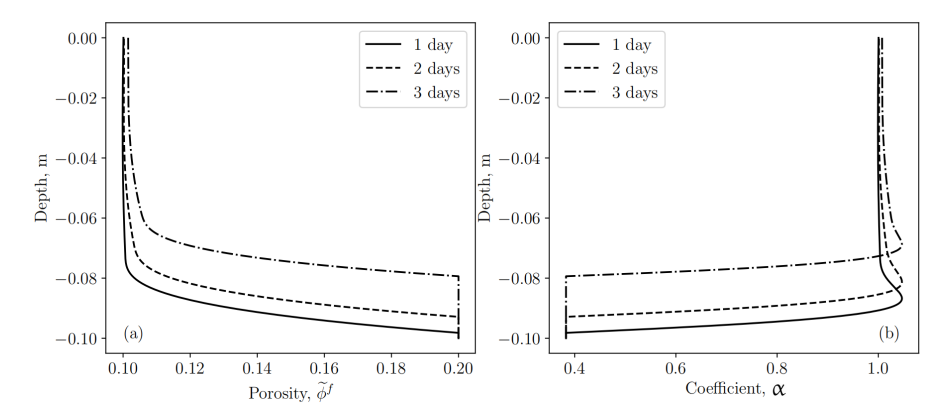
Fig. 2. Layout of the configuration for the Terzaghi problem.

Table 1. Parameters used in the simulation of the Terzaghi consolidation problem.

	Aniso. Mat.	$\operatorname{Unit}$
Elasticity:		
$\lambda$	4270	MPa
a	-1870	MPa
b	5420	-
$\mu_T$	9360	MPa
$\mu_L$	6510	MPa
Fluid flow:		
$\kappa_{\parallel}$	1	$\mu { m D}$
$\kappa_{\perp}$	0.1	$\mu { m D}$
$\mu_w$	1	cP
Internal erosion:		
$n_{\perp}$	3	-
$n_{\parallel}$	3	-
$A^{"}$	5000	-
B	$1.00 \times 10^{-4}$	$kg/m^3/s$
C	$9.93 \times 10^{-5}$	$kg/m^3/s$
$K_{sr}$	42996.7	MPa
$K_f$	2000	MPa
$\vec{K_{se}}$	40000	MPa
$ ho_{sr}$	2400	$\mathrm{kg/m^3}$
$ ho_{se}$	2000	$kg/m^3$

excess pore pressure takes longer to dissipate, and so a higher rate of internal erosion is sustained for a longer period of time.

During the consolidation process the parameter  $\alpha$  defined in equation (50) varies as shown in Figure 3b. As suggested in the figure, when the solid concentration in the fluid is low the overall hydraulic conductivity is high due to the increased intrinsic permeability ( $\alpha > 1$ ). But as more and more solid dissolves and mixes with the fluid, the fluid viscosity increases to such a point that the overall permeability of the material decreases ( $\alpha < 1$ ). Note that the amount at which the porosity increases and the amount at which  $\alpha$  decreases are limited by the amount of soluble solid in the material.



**Fig. 3.** (a) Porosity after 1, 2, 3 days of consolidation for the case  $B = 1 \times 10^{-4}$  g/mm<sup>3</sup>/day; (b) Coefficient  $\alpha$  after 1, 2, 3 days of consolidation for the case  $B = 1 \times 10^{-4}$  g/mm<sup>3</sup>/day.

Next, we vary the parameter B and illustrate how it impacts the evolution of ground settlement and the pore pressure dissipation. Figure 4 shows the results of the sensitivity analysis. As displayed in Figure 4a, the higher the value of B, the faster the solid dissolves, resulting in the degradation of stiffness and larger ground settlement. On the other hand, as suggested in Figure 4b, even if the excess pore pressures for all values of B dissipate to zero, the case with the higher value of B causes more solid to dissolve and the hydraulic conductivity to decrease, resulting in a slower rate of excess pore pressure dissipation. For reference, the benchmark Terzaghi solution (without erosion) is also shown in these two figures. In this case, erosion results in greater settlement due to porosity increase, and slower pore pressure dissipation due to increased viscosity of the fluid.

#### 4.2 Reactive fluid injection into transversely isotropic rock

In shale gas exploitation, reactive fluid such as hydrochloric acid is usually injected to the reservoir prior to hydraulic fracturing to increase the hydraulic

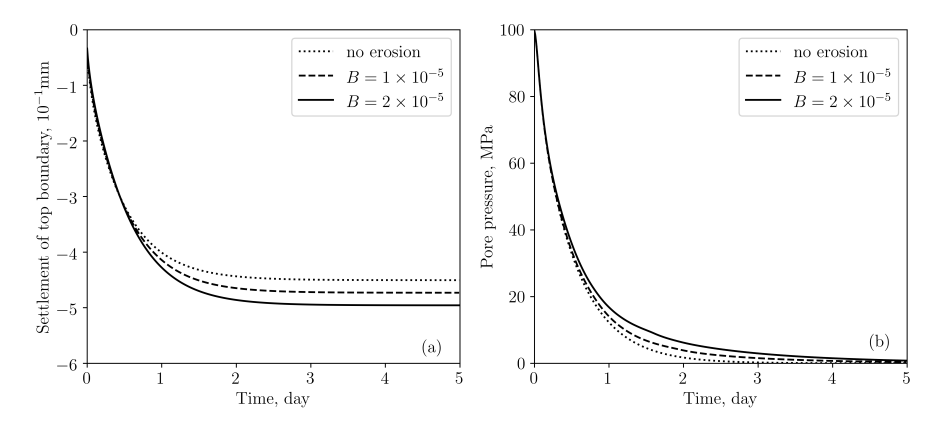


**Fig. 4.** Evolutions of (a) ground settlement and (b) pore pressure at midheight with time for different values of B.

conductivity as well as reduce the strength and stiffness of the shale rock. In this example, we conduct a plane strain simulation of the reactive fluid injection process into a stratum of transversely isotropic porous rock revealing the impact of internal erosion on the hydromechanical response of the rock.

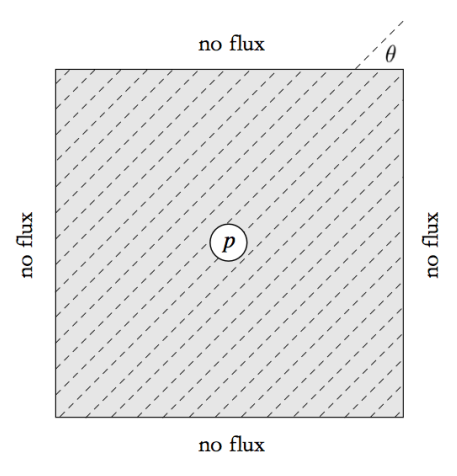


Fig. 5. Geometry and boundary conditions for the reactive fluid injection problem.

The simulation domain for this problem is a  $10 \text{m} \times 10 \text{m}$  square region. A wellbore with a radius of 0.5 m is inserted in the center of the domain. The injected fluid in the wellbore exerts a perpendicular pressure of 0.5 MPa on the interior boundary. The outer boundaries of the domain are all impermeable and supported with rollers. A diagram of the layout of this example is

portrayed in Figure 5. The plane of isotropy of the reservoir rock is denoted by the angle  $\theta=45^{\circ}$ . The parameters for this example are the same as in the first example reported in Table 1, except that  $B=1.0\times 10^{-5}$  and  $C=9.93\times 10^{-6}$  (both in kg/m³/s). We assume that the volume fraction of the solid that is not soluble is 0.8, which means that the maximum concentration of dissolved solid in the fluid is 0.5.

To demonstrate the influence of internal erosion on the hydromechanical response of the rock, the pore pressure contours at a common post-injection time for cases with and without internal erosion are reported in Figure 6. As shown in the figure, the fluid flow along the plane of isotropy is more prominent since the permeability on this plane is higher than in the normal direction. We also see that the fluid containing dissolved solid finds it more difficult to permeate into the surrounding rock due to the increased viscosity.

The material in this example is stiffer along the plane of isotropy than in the direction perpendicular to this plane, so when the pressure inside the wellbore is applied more stretching is noted in the perpendicular direction. This induces a dilative volumetric strain along the plane of isotropy, as shown in Figure 7a, which facilitates internal erosion. The end result is a higher concentration of dissolved solid on the plane of isotropy, as shown in Figure 7b.

Lastly, Figures 8(a), (b), and (c) show the evolution of solid concentration  $\psi^e$  with time, and (d) damage due to erosion. Starting near the wellbore, the zone of erosion propagates mostly in the diagonal direction parallel to the plane of isotropy. However, the thickness of the zone of erosion also increases with time, which means that the solid also dissolves in the direction perpendicular to the plane of isotropy. Note that the distribution of damage due to erosion very much resembles the concentration of dissolved solid.

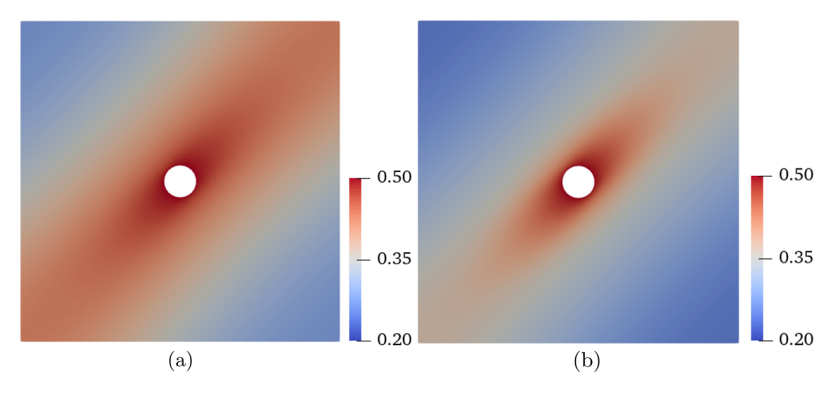


**Fig. 6.** Contour of: (a) pore pressure without internal erosion, and (b) pore pressure considering internal erosion. Both contours taken at t=1.527 days.

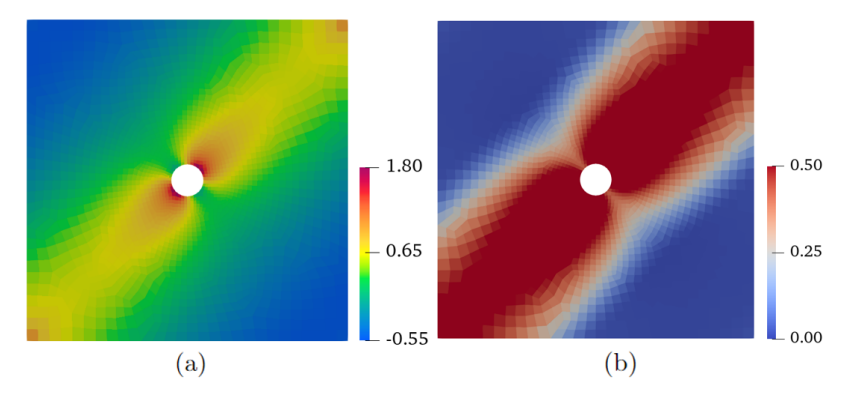


**Fig. 7.** Contour of: (a) volumetric strain (color bar  $\times 10^{-5}$ ), and (b) concentration of dissolved solid. Both contours taken at t = 1.527 days.

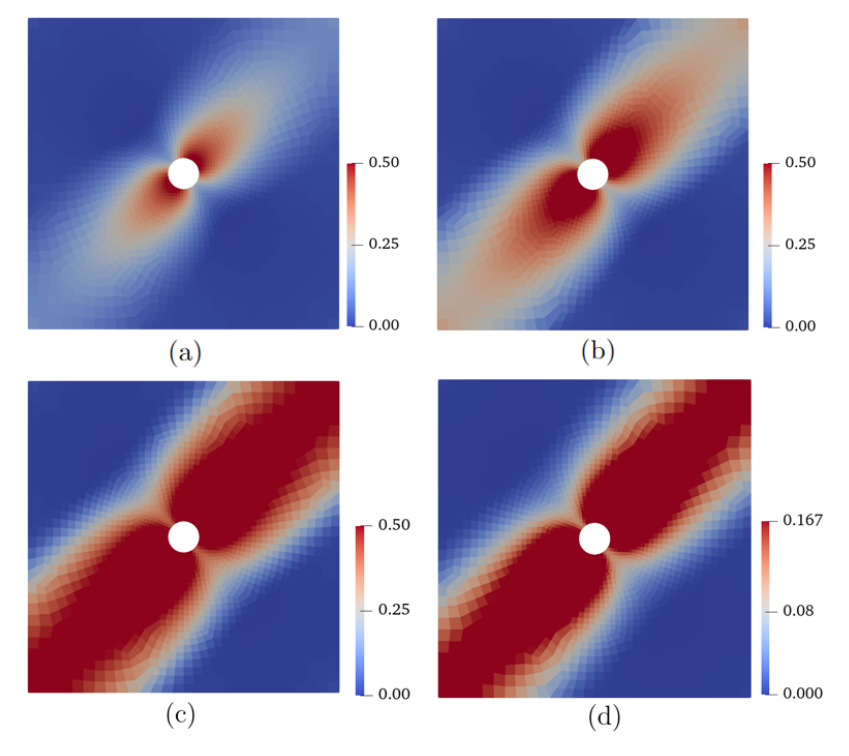


**Fig. 8.** Contour of concentration of dissolved solid: (a) t=0.317 days, (b) t=0.623 days, and (c) t=1.527 days; and (d) damage due to erosion at t=1.527 days.

## 4.3 Acidic water-induced weathering of calcarenites

When exposed to water or an acidic environment, carbonatic rocks such as calcarenites are soluble, and solid dissolution and damage may occur due to

chemical reaction. Underground cavities and karst caves are the products of the long-term effects of this process [18].

Ciantia and Hueckel [13] conducted a series of weathering experiments on submerged stressed calcarenites. As the investigated rock specimen first underwent solid dissolution, the alteration of mechanical properties of the specimen was recorded at different reaction times. The experiment showed that solid dissolution led to stiffness degradation in the rock, and an approximately linear dependence of the stiffness on the porosity was observed. This phenomenon was explained from the fact that calcarenites are considered as bonded geomaterials, and solid dissolution compromised the bond which leads to degradation of the stiffness. To study the mixed effects of saturation and chemical dissolution, as well as to monitor the process of grain dissolution, Ciantia et al. [12] conducted additional experiments on calcarenites in water with different pH. They then analyzed the impact of rate of dissolution on the hydromechanical behavior of the rock.

**Table 2.** Parameters used in the simulation of the dissolution of calcarenites.

	Iso. Mat.	Unit
Elasticity:		
$\lambda$	70	MPa
a	0	MPa
b	0	-
$\mu_T$	104	MPa
$\mu_L$	104	MPa
Fluid flow:		
$\kappa_{\parallel}$	0.1	D
$\kappa_{\perp}^{"}$	1	D
$\mu_w$	1	cP
Internal erosion:		
$n_{\perp}$	3	-
$n_{\parallel}$	3	-
$A^{"}$	1000	-
B	$5.00 \times 10^{-3}$	$kg/m^3/s$
C	$4.97 \times 10^{-3}$	$kg/m^3/s$
$K_{se}$	2200	MPa
$K_f$	2000	MPa
$K_{sr}$	2400	MPa
$ ho_{sr}$	2400	$\mathrm{kg/m}^3$
$ ho_{se}$	2000	${ m kg/m^3}$

To simulate the weathering experiments on the calcarenites, we use a 2D plane strain representation of the sample as depicted in Figure 9. The rectangular domain is 38 mm wide and 76 mm tall [12, 13] with the lateral and bottom boundaries supported on rollers. No flux boundary is applied on the

lateral and bottom boundaries, and fluid may only drain to the top boundary. An overburden stress of  $\omega = 1.6$  MPa was applied on the top boundary.

The model parameters used in this problem are tabulated in Table 2. The mechanical properties of the calcarenites were derived from the experiment on intact calcarenites [13, 63], while the permeability parameter was chosen from Andriani and Walsh [1]. To fit the experimental curve, the water-induced dissolution rate was taken as  $B = 5.0 \times 10^{-3} \text{ kg/m}^3/\text{s}$ , while the acidic fluid-induced dissolution rate was taken as  $B = 1.0 \times 10^{-2} \text{ kg/m}^3/\text{s}$ .

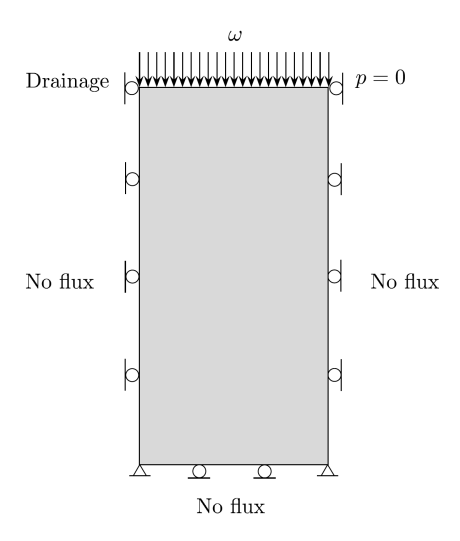


Fig. 9. Layout of the weathering experiment on calcarenites.

Ciantia et al. [12] observed that solid dissolution degraded the stiffness of the calcarenites by dissolving the bond, gradually converting the rock into granular soils. Based on this information, we introduce an additional parameter  $\xi$  representing the volume fraction of the bond in the intact solid, and modify the damage law as

$$\dot{D}_e = \frac{\dot{m}_s}{\xi \rho_{sr}} \,, \tag{71}$$

where the parameter  $\xi$  is chosen as 0.1 in this example. To validate the damage and dissolution laws, we replicate the experimental results reported by Ciantia and Hueckel [13] and plot the evolution of the percentage of dissolved solid and the stiffness degradation in Figure 10.

In plotting Figure 10a, we should note that the dissolution rate is not uniform across the domain because the hydromechanical response of the sample was solved as a boundary-value problem. Thus, to compare with the exper-



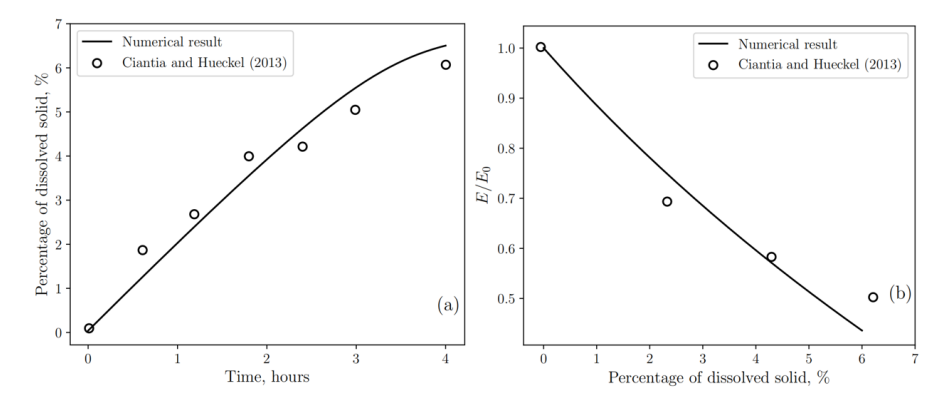


Fig. 10. Weathering experiment on calcarenites: (a) evolution of the percentage of dissolved solid, and (b) dependence of stiffness degradation on the dissolution.

imental observations we calculate the volume average of the percentage of dissolved solid, which is given by the integral

$$\frac{1}{V} \int_{\mathcal{O}} \frac{\Delta \phi^{se}}{\phi^{sr} + \phi^{se}} dV$$
,

where  $\phi^{sr} + \phi^{se}$  is the initial volume fraction of the solid, and V is the total volume of the sample. In plotting Figure 10b, we load the sample vertically after dissolution considering the heterogeneous distribution of material stiffness at different reaction times. We then obtain the material stiffness from the tangent of the vertical stress-vertical strain curve. From Figure 10a, we find that the calculated rate of dissolution decreases with reaction time, in agreement with the experiment. The reason for this is because the volume fraction of the remaining soluble solid decreases with reaction time. On the other hand, as the sample consolidates and more and more compressive load is transferred to the solid skeleton, the rate of dissolution also decreases.

To better capture the coupled effect of saturation and chemical dissolution with different types of fluids, we conduct a dissolution simulation on calcarenites with a loading protocol consisting of four chemo-mechanical loading steps. The results are shown in Figure 11. In the first step, the rock sample is loaded without saturation at the value  $\omega=1.6$  MPa (OA). Then, water is added in the second step (AB) as the sample is loaded further to point B. During this step, the slope of the curve does not change much since the effect of water-induced dissolution is small compared to the deformation induced by the mechanical load. For the third step, the sample is allowed to dissolve from water saturation, causing the vertical strain to increase slightly (BC). For the fourth step, acid is introduced into the solution at point C, resulting in the vertical strain to increase at a faster rate (CD). Capturing the faster rate of dissolution under an acidic environment requires that the dissolution

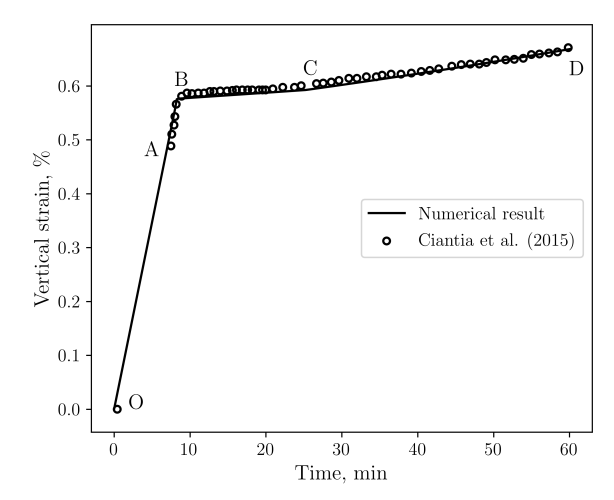


Fig. 11. Evolution of the vertical strain at different stages of chemo-mechanical loading.

rate parameter B be increased from  $5 \times 10^{-3}$  kg/m<sup>3</sup>/s for water saturation to  $1 \times 10^{-2}$  kg/m<sup>3</sup>/s for saturation with an acidic solution.

To further elucidate the dissolution process, Figure 12 plots the profiles of the pore pressure and porosity along the centerline at various reaction times. During the consolidation process, the pore fluid gradually drains through the top surface, causing the pore pressure to dissipate with time at a faster rate on top than at the bottom of the sample. This results in nonuniform distribution of effective stress and nonuniform dissolution rates across the height of the sample. From Figure 12b, we see that the dissolution rate at the bottom of the sample is faster, resulting in increased porosity. This can be explained from the fact that the lower effective stress at the bottom of the sample results in smaller compressive volumetric strain, which means that more pore spaces are left open for the fluid to infiltrate and dissolve the solid. We note that this simulation assumes that there is continuous supply of reactive agents that dissolve the solid. Otherwise, the balance of chemical concentration must be enforced in the model formulation. This latter topic is currently being incorporated into the mathematical framework.

## 5 Closure

We have formulated a mathematical framework for solid-fluid interaction in porous materials with internal erosion based on mixture theory and continuum thermodynamics. The mixture of the pore fluid and dissolved solid was treated as a thick fluid whose viscosity increases with the concentration of dissolved solid. Regarding internal erosion, we considered the case where internal

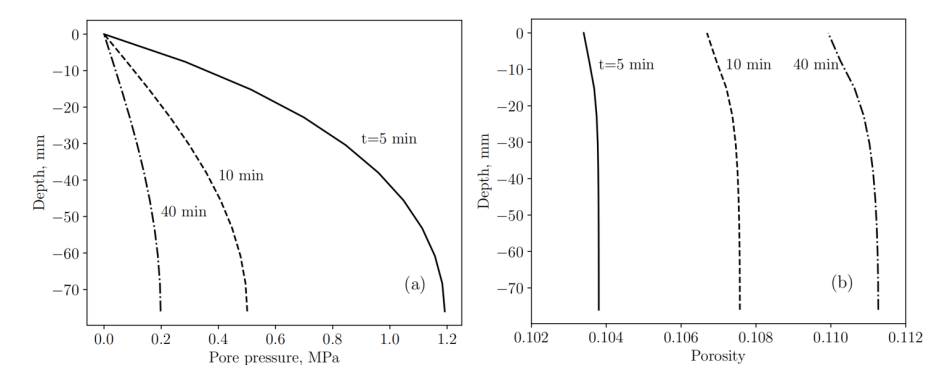


Fig. 12. Evolution of: (a) pore pressure, and (b) porosity.

erosion is induced by chemical reaction and proposed a phenomenological expression for the rate of solid dissolution as a function of the volumetric strain. A chemical damage variable  $D_e$  was introduced to account for the stiffness degradation induced by solid dissolution. The classic  $\boldsymbol{u}/p$  formulation with mass exchanges was used to solve the problem.

Three numerical examples were presented to highlight the impact of internal erosion on the hydromechanical responses of geologic systems undergoing solid dissolution. The examples include a modified Terzaghi 1D consolidation problem with internal erosion,  $CO_2$  injection into a transversely isotropic rock, and weathering experiment on calcarenites. The results highlighted the interplay between mechanical deformation, fluid flow, and chemical reaction. Although not directly addressed in this paper, thermal effects could also play a significant role in the system response in the sense that the rate of internal erosion parameters B and C generally depend on temperature and pH. Lastly, one aspect not considered in this paper is the propagation of fractures induced by solid dissolution. We are currently working on this topic and will report progress in future publications.

#### Acknowledgments

Support for this work was provided by the National Science Foundation under Award Number CMMI-1914780 and by the U.S. Department of Energy, Office of Science, Office of Basic Energy Sciences, Geosciences Research Program, under Award Number DE-FG02-03ER15454.

# Appendix A. Tangent operator

In this appendix, we summarize the expressions for the tangent operators used with Newton iteration to solve the nonlinear coupled system. Denoting

the permeability matrix as  $\kappa$ , the submatrix  $\mathbf{K}_{ij}$  in the tangent matrix for a Newton-Raphson iteration loop takes the following forms:

$$\mathbf{K}_{11} = \frac{\partial \mathbf{R}_{u}}{\partial \mathbf{d}} = \int_{\mathcal{B}} \mathbf{B}^{\mathsf{T}} \frac{\partial \{\mathbf{\sigma}'\}}{\partial \{\mathbf{\varepsilon}\}} \mathbf{B} \, dV + \int_{\mathcal{B}} \frac{\partial \mathbf{N}_{u}^{\mathsf{T}} \dot{m}^{s}}{\partial \mathbf{d}} \frac{\mathbf{q}}{\phi_{n}^{f}} \, dV \,, \tag{72a}$$

$$= \int_{\mathcal{B}} \mathbf{B}^{\mathsf{T}} \mathbf{C}^{e} \mathbf{B} \, dV + \int_{\mathcal{B}} \mathbf{N}_{u}^{\mathsf{T}} \phi_{n}^{sr} A (B - C) \exp(-A \varepsilon_{v}) \frac{\mathbf{q}}{\phi_{n}^{f}} \mathbf{1}^{\mathsf{T}} \mathbf{B} \, dV \,. \tag{72b}$$

$$\mathbf{K}_{12} = \frac{\partial \mathbf{R}_{u}}{\partial p} = -\int_{\mathcal{B}} \mathbf{B}^{\mathsf{T}} \mathbf{b} \mathbf{N}_{p} \, dV + \int_{\mathcal{B}} \frac{\partial \mathbf{N}_{u}^{\mathsf{T}} \dot{m}^{s} (\mathbf{v}_{f} - \mathbf{v})}{\partial p} \, dV \,, \tag{72b}$$

$$= -\int_{\mathcal{B}} \mathbf{B}^{\mathsf{T}} \mathbf{b} \mathbf{N}_{p} \, dV + \int_{\mathcal{B}} \frac{\mathbf{N}_{u}^{\mathsf{T}} \dot{m}^{s} \mathbf{E}}{\phi_{n}^{f}} \, dV \,, \tag{72b}$$

$$\mathbf{K}_{21} = \frac{\partial \mathbf{R}_{p}}{\partial \mathbf{d}} = \int_{\mathcal{B}} \mathbf{N}_{p}^{\mathsf{T}} \mathbf{b} \mathbf{B} \, dV + \left(\frac{1}{\rho_{sr}} - \frac{1}{\rho_{se}}\right) \int_{\mathcal{B}} \frac{\partial \mathbf{N}_{p}^{\mathsf{T}} \dot{m}^{s}}{\partial \mathbf{d}} \, dV \,, \tag{72c}$$

$$= \int_{\mathbf{B}} \mathbf{N}_{p}^{\mathsf{T}} \mathbf{b} \mathbf{B} \, dV + \left(\frac{1}{\rho_{sr}} - \frac{1}{\rho_{se}}\right) \int_{\mathcal{B}} \mathbf{N}_{p}^{\mathsf{T}} \phi_{n}^{sr} A (B - C) \exp(-A \varepsilon_{v}) \mathbf{1} \mathbf{B} \, dV \,, \tag{72c}$$

$$\mathbf{K}_{22} = \frac{\partial \mathbf{R}_{p}}{\partial p} = \int_{\mathcal{B}} \frac{\Delta t}{\mu_{f}} \mathbf{E} \mathbf{K} \mathbf{E} \, dV + \int_{\mathcal{B}} \frac{1}{\mathcal{M}_{n}} \mathbf{N}_{p}^{\mathsf{T}} \mathbf{N}_{p} \, dV \,, \tag{72c}$$

$$+ \int_{\mathcal{B}} \left(\frac{\psi_{n}^{f}}{K_{f}} + \frac{\psi_{n}^{se}}{K_{ce}}\right) \Delta t \mathbf{N}_{p}^{\mathsf{T}} \mathbf{q} \mathbf{E} \, dV - \int_{\mathcal{B}} \left(\frac{\psi_{n}^{f}}{K_{f}} + \frac{\psi_{n}^{se}}{K_{ce}}\right) \frac{\Delta t}{\mu_{v}} \mathbf{N}_{p}^{\mathsf{T}} \nabla p \cdot \mathbf{K} \mathbf{E} \, dV \,. \tag{72c}$$

# Data availability statement

The datasets generated during the course of this study are available from the corresponding author upon reasonable request.

#### References

- [1] Andriani G, Walsh N (2003). Fabric, porosity and water permeability of calcarenites from Apulia (SE Italy) used as building and ornamental stone. Bulletin of Engineering Geology and the Environment 62(1):77–84.
- [2] Audigane P, Gaus I, Czernichowski-Lauriol I, Pruess K, Xu T (2007). Two-dimensional reactive transport modeling of CO<sub>2</sub> injection in a saline aquifer at the Sleipner site, North Sea. American Journal of Science 307(7):974–1008.

- [3] Bennett KC, Berla LA, Nix WD, Borja RI (2015). Instrumented nanoindentation and 3D mechanistic modeling of a shale at multiple scales. Acta Geotechnica 10(1):1–14.
- [4] Borja RI, Alarcón E (1995). A mathematical framework for finite strain elastoplastic consolidation Part 1: Balance laws, variational formulation, and linearization. Computer Methods in Applied Mechanics and Engineering 122(1-2):145–171.
- [5] Borja RI, Tamagnini C, Alarcón E (1998). Elastoplastic consolidation at finite strain Part 2: Finite element implementation and numerical examples. Computer Methods in Applied Mechanics and Engineering 159(1-2):103–122.
- [6] Borja RI (2013). Plasticity Modeling & Computation. Springer, Berlin-Heidelberg.
- [7] Borja RI, Choo J (2016). Cam-Clay plasticity, Part VIII: A constitutive framework for porous materials with evolving internal structure. Computer Methods in Applied Mechanics and Engineering 309:653–679.
- [8] Borja RI, Yin Q, Zhao Y (2020). Cam-Clay plasticity. Part IX: On the anisotropy, heterogeneity, and viscoplasticity of shale. Computer Methods in Applied Mechanics and Engineering 360:112695.
- [9] Borja RI (2022). Computational Poromechanics, Lecture Notes, Stanford University.
- [10] Borja RI, Chen W, Odufisan AR (2023), A constitutive framework for rocks undergoing solid dissolution. Journal of the Mechanics and Physics of Solids 73:105198.
- [11] Carroll SA, McNab WW, Dai Z, Torres SC (2013). Reactivity of Mount Simon sandstone and the Eau Claire shale under  $CO_2$  storage conditions. Environmental Science & Technology 47(1):252–261.
- [12] Ciantia MO, Castellanza R, Di Prisco C (2015). Experimental study on the water-induced weakening of calcarenites. Rock Mechanics and Rock Engineering 48(2):441–461.
- [13] Ciantia MO, Hueckel T (2013). Weathering of submerged stressed calcarenites: chemo-mechanical coupling mechanisms. Géotechnique 63(9):768–785.
- [14] Civan F (2002). Relating permeability to pore connectivity using a power-law flow unit equation. Petrophysics-The SPWLA Journal of Formation Evaluation and Reservoir Description 43(06).
- [15] Costa A (2016). Permeability-porosity relationship: A reexamination of the Kozeny-Carman equation based on a fractal pore-space geometry assumption. Geophysical Research Letters 33(2).
- [16] Coussot P (1997). Mudflow Rheology and Dynamics. Balkema, Rotterdam.
- [17] Coussy O (2004). Poromechanics. John Wiley & Sons.
- [18] Culshaw MG, Maltham AC (1987). Natural and artificial cavities as ground engineering hazards. Quarterly Journal of Engineering Geology and Hydrogeology 20(2):139–150.

- [19] Ellis B, Peters C, Fitts J, Bromhal G, McIntyre D, Warzinski R, Rosenbaum E (2011). Deterioration of a fractured carbonate caprock exposed to CO<sub>2</sub>-acidified brine flow. Greenhouse Gases: Science and Technology 1(3):248–260.
- [20] Eubanks RA, Sternberg E (1954). On the axisymmetric problem of elasticity theory for a medium with transverse isotropy. Journal of Rational Mechanics and Analysis 3:89–101.
- [21] Fell R, Wan CF, Cyganiewicz J, Foster M (2003). Time for development of internal erosion and piping in embankment dams. Journal of Geotechnical and Geoenvironmental Engineering 129(4):307–314.
- [22] Flores-Berrones R, Ramírez-Reynaga M, Macari EJ (2011). Internal erosion and rehabilitation of an earth-rock dam. Journal of Geotechnical and Geoenvironmental Engineering 137(2):150–160.
- [23] Friedson AJ, Stevenson DJ (1983). Viscosity of rock-ice mixtures and applications to the evolution of icy satellites. Icarus 56(1):1–14.
- [24] Garbis SJ, Taylor JL (1986). The utility of CO<sub>2</sub> as an energizing component for fracturing fluids. SPE Production Engineering 1(05):351–358.
- [25] Gaus I (2010). Role and impact of CO<sub>2</sub>-rock interactions during CO<sub>2</sub> storage in sedimentary rocks. International Journal of Greenhouse Gas Control 4(1):73–89.
- [26] Gelet R, Kodieh A, Marot D, Nguyen N-S (2021). Analysis of volumetric internal erosion in cohesionless soils: Model, experiments and simulations International Journal for Numerical and Analytical Methods in Geomechanics 45(18):2780–2806.
- [27] Ghanbarian B, Male F (2021). Theoretical power-law relationship between permeability and formation factor. Journal of Petroleum Science and Engineering 198:108249.
- [28] Harvey OR, Qafoku NP, Cantrell KJ, Lee G, Amonette JE, Brown CF (2013). Geochemical implications of gas leakage associated with geologic CO<sub>2</sub> storage—A qualitative review. Environmental Science & Technology 47(1):23–36.
- [29] Hitchon B (1996). Aquifer Disposal of Carbon Dioxide: Hydrodynamic and Mineral Trapping–Proof of Concept. Geoscience Publishing Ltd., Alberta, Canada.
- [30] Holtz R, Kovacs WD (1981). An Introduction to Geotechnical Engineering, Prentice-Hall. New Jersey.
- [31] Hu M, Hueckel T (2019). Modeling of subcritical cracking in acidized carbonate rocks via coupled chemo-elasticity. Geomechanics for Energy and the Environment 19:100114.
- [32] Ip SCY, Choo J, Borja RI (2021). Impacts of saturation-dependent anisotropy on the shrinkage behavior of clay rocks. Acta Geotechnica 16(11):3381–3400.
- [33] Ip SCY, Borja RI (2022). Evolution of anisotropy with saturation and its implications for the elastoplastic responses of clay rocks. Interna-

- tional Journal for Numerical and Analytical Methods in Geomechanics 46(1):23-46.
- [34] Ip SCY, Borja RI (2022). A phase-field approach for compaction band formation due to grain crushing. International Journal for Numerical and Analytical Methods in Geomechanics 46(16):2965–2987.
- [35] Jiang Y, Luo Y, Lu Y, Qin C, Liu H (2016). Effects of supercritical CO<sub>2</sub> treatment time, pressure, and temperature on microstructure of shale. Energy 97:173–181.
- [36] Jun YS, Giammar DE, Werth CJ (2013). Impacts of geochemical reactions on geologic carbon sequestration. Environmental Science & Technology 47(1):3–8.
- [37] Kobayashi I, Owada H, Ishii T, Iizuka A (2017). Evaluation of specific surface area of bentonite-engineered barriers for Kozeny-Carman law. Soils and Foundations 57(5):683–697.
- [38] Lasaga AC (1984). Chemical kinetics of water-rock interactions. Journal of Geophysical Research: Solid Earth 89(B6):4009–4025.
- [39] Lasaga AC (2014). Kinetic Theory in the Earth Sciences. Princeton University Press.
- [40] Latief FDE, Fauzi U (2012). Kozeny-Carman and empirical formula for the permeability of computer rock models. International Journal of Rock Mechanics and Mining Sciences 50:117–123.
- [41] Lee SY, Hyder LK, Alley PD (1991). Microstructural and mineralogical characterization of selected shales in support of nuclear waste repository studies. In: Microstructure of Fine-Grained Sediments. Frontiers in Sedimentary Geology. Springer, New York, NY.
- [42] Li L, Rivas E, Gracie R, Dusseault MB (2021). Methodology for the nonlinear coupled multi-physics simulation of mineral dissolution. International Journal for Numerical and Analytical Methods in Geomechanics 45(15):2193–2213.
- [43] Li W, Sun Y, Xin M, Bian R, Wang H, Wang YN, Hu Z, Linh HN, Zhang D (2020). Municipal solid waste incineration fly ash exposed to carbonation and acid rain corrosion scenarios: Release behavior, environmental risk, and dissolution mechanism of toxic metals. Science of the Total Environment 744:140857.
- [44] Liu D, Li Y, Yang S, Agarwal RK (2021). CO<sub>2</sub> sequestration with enhanced shale gas recovery. Energy Sources, Part A: Recovery, Utilization, and Environmental Effects 43(24):3227–3237.
- [45] Liu F, Lu P, Griffith C, Hedges SW, Soong Y, Hellevang H, Zhu C (2012). CO<sub>2</sub>-brine-caprock interaction: Reactivity experiments on Eau Claire shale and a review of relevant literature. International Journal of Greenhouse Gas Control 7:153–167.
- [46] Luo Y, Luo B, Xiao M (2020). Effect of deviator stress on the initiation of suffusion. Acta Geotechnica 15(6):1607–1617.

- [47] Lyu Q, Ranjith PG, Long X, Ji B (2016). Experimental investigation of mechanical properties of black shales after CO<sub>2</sub>-water-rock interaction. Materials 9(8):663.
- [48] Malvern LE (1969). Introduction to the Mechanics of a Continuous Medium. Prentice-Hall, Inc., Englewood Cliffs, NJ.
- [49] Middleton R, Viswanathan H, Currier R, Gupta R (2014). CO<sub>2</sub> as a fracturing fluid: Potential for commercial-scale shale gas production and CO<sub>2</sub> sequestration. Energy Procedia 63:7780–7784.
- [50] Min T, Gao Y, Chen L, Kang Q, Tao WW (2016). Changes in porosity, permeability and surface area during rock dissolution: effects of mineralogical heterogeneity. International Journal of Heat and Mass Transfer 103:900–913.
- [51] Mooney M (1951). The viscosity of a concentrated suspension of spherical particles. Journal of Colloid Science 6(2):162–170.
- [52] Orr FM (2018). Carbon capture, utilization, and storage: an update. SPE Journal 23(03):2444–2455.
- [53] Pechukas P (1981). Transition state theory. Annual Review of Physical Chemistry 32(1):159–177.
- [54] Reeves SR (2001). Geological sequestration of CO<sub>2</sub> in deep, unmineable coalbeds: an integrated research and commerical-scale field demonstration project. In SPE Annual Technical Conference and Exhibition. OnePetro.
- [55] Rice PA, Fontugne DJ, Latini RG, Barduhn AJ (1970). Anisotropic permeability in porous media. Industrial & Engineering Chemistry 62(6):23– 31
- [56] Richards KS, Reddy KR (2007). Critical appraisal of piping phenomena in earth dams. Bulletin of Engineering Geology and the Environment 66(4):381-402.
- [57] Rochelle CA, Czernichowski-Lauriol I, Milodowski AE (2004). The impact of chemical reactions on CO<sub>2</sub> storage in geological formations: a brief review. Geological Society, London, Special Publications 233(1):87–106.
- [58] Rohmer J, Pluymakers A, Renard F (2016). Mechano-chemical interactions in sedimentary rocks in the context of CO<sub>2</sub> storage: Weak acid, weak effects? Earth-Science Reviews 157:86–110.
- [59] Rutter EH (1983). Pressure solution in nature, theory and experiment. Journal of the Geological Society 140(5):725–740.
- [60] Scheperboer IC, Suiker ASJ, Bosco E, Clemens FHLR (2022). A coupled hydro-mechanical model for subsurface erosion with analyses of soil piping and void formation. Acta Geotechnica 17:4769–4798.
- [61] Scheperboer (2023). Condition Assessment of Concrete Sewer Pipes through an Integrated Experimental-Numerical Approach. Bouwstenen 349, Eindhoven University of Technology, The Netherlands.
- [62] Semnani SJ, White JA, Borja RI (2016). Thermoplasticity and strain localization in transversely isotropic materials based on anisotropic crit-

- ical state plasticity. International Journal for Numerical and Analytical Methods in Geomechanics 40(18):2423–2449.
- [63] Sharifi J, Saberi MR, Javaherian A, Hafezi MN (2021). Investigation of static and dynamic bulk moduli in a carbonate field. Exploration Geophysics 52(1):16-41.
- [64] Shwiyhat N, Xiao M (2010). Effect of suffusion on mechanical characteristics of sand. Scour and Erosion 378–386.
- [65] Smith MB, Montgomery C (2015). Hydraulic fracturing. CRC press.
- [66] Sone H, Zoback MD (2013). Mechanical properties of shale-gas reservoir rocks—Part 1: Static and dynamic elastic properties and anisotropy. Geophysics 78(5):D381–D392.
- [67] Song X, Borja RI (2014). Mathematical framework for unsaturated flow in the finite deformation range. International Journal for Numerical Methods in Engineering 97(9):658–682.
- [68] Spencer AJM (2014). Continuum theory of the mechanics of fibrereinforced composites (Vol. 282). Springer.
- [69] Spyropoulos C, Griffith WJ, Scholz CH, Shaw BE (1999). Experimental evidence for different strain regimes of crack populations in a clay model. Geophysical Research Letters. 26(8):1081–1084.
- [70] Stavropoulou M, Papanastasiou P, Vardoulakis I (1998). Coupled well-bore erosion and stability analysis. International Journal for Numerical and Analytical Methods in Geomechanics 22(9):749–769.
- [71] Ulm FJ, Abousleiman Y (2006). The nanogranular nature of shale. Acta Geotechnica 1(2):77–88.
- [72] Wang Y, Borja RI, Wu W (2023). Dynamic strain localization into a compaction band via a phase-field approach. Journal of the Mechanics and Physics of Solids 173:105228.
- [73] Wei W, Cai J, Xiao J, Meng Q, Xiao B, Han Q (2018). Kozeny-Carman constant of porous media: Insights from fractal-capillary imbibition theory. Fuel 234:1373–1379.
- [74] White JA, Borja RI (2008), Stabilized low-order finite elements for coupled solid-deformation/fluid-diffusion and their application to fault zone transients. Computer Methods in Applied Mechanics and Engineering 197:4353–4366.
- [75] Wu W, Sharma MM (2017). Acid fracturing in shales: effect of dilute acid on properties and pore structure of shale. SPE Production & Operations 32(01):51–63.
- [76] Yürüm Y, Dror Y, Levy M (1985). Effect of acid dissolution on the mineral matrix and organic matter of Zefa EFE oil shale. Fuel Processing Technology 11(1):71–86.
- [77] Zhang Q (2020). Hydromechanical modeling of solid deformation and fluid flow in the transversely isotropic fissured rocks. Computers and Geotechnics 128:103812.

- [78] Zhang Y, He J, Li X, Lin C (2019). Experimental study on the supercritical CO<sub>2</sub> fracturing of shale considering anisotropic effects. Journal of Petroleum Science and Engineering 173:932–940.
- [79] Zhang Q, Yan X, Shao J (2021). Fluid flow through anisotropic and deformable double porosity media with ultra-low matrix permeability: A continuum framework. Journal of Petroleum Science and Engineering 200:108349.
- [80] Zhang Q, Choo J, Borja RI (2019). On the preferential flow patterns induced by transverse isotropy and non-Darcy flow in double porosity media. Computer Methods in Applied Mechanics and Engineering 353:570–592.
- [81] Zhang Q, Borja RI (2021). Poroelastic coefficients for anisotropic single and double porosity media. Acta Geotechnica 16(10):3013–3025.
- [82] Zhao Y, Borja RI (2020). A continuum framework for coupled solid deformation-fluid flow through anisotropic elastoplastic porous media. Computer Methods in Applied Mechanics and Engineering 369:113225.
- [83] Zhao Y, Borja RI (2021). Anisotropic elastoplastic response of doubleporosity media. Computer Methods in Applied Mechanics and Engineering 380:113797.
- [84] Zhao Y, Borja RI (2022). A double-yield-surface plasticity theory for transversely isotropic rocks. Acta Geotechnica, https://doi.org/10.1007/s11440-022-01605-6.
- [85] Zhao C, Hobbs BE, Ord A (2016). Chemical dissolution-front instability associated with water-rock reactions in groundwater hydrology: Analyses of porosity-permeability relationship effects. Journal of Hydrology 540:1078–1087.
- [86] Zhao Y, Semnani SJ, Yin Q, Borja RI (2018). On the strength of transversely isotropic rocks. International Journal for Numerical and Analytical Methods in Geomechanics 42(16):1917–1934.
- [87] Zhao Y, Wang R, Zhang JM (2022). A dual-mechanism tensile failure criterion for transversely isotropic rocks. Acta Geotechnica, https://doi.org/10.1007/s11440-022-01604-7.
- [88] Znidarcic D, Schiffman RL (1982). On Terzaghi's concept of consolidation. Géotechnique 32(4):387–389.